Available online at www.sciencedirect.com
ScienceDirect
Journal of Power Sources 160 (2006) 1111–1121
JOURNAL OF POWER SOURCES
www.elsevier.com/locate/jpowsour

Numerical simulation of a mini PEMFC stack

Zhixiang Liu [a], Zongqiang Mao [a,*], Cheng Wang [a], Weilin Zhuge [b], Yangjun Zhang [b]

[a] *Institute of Nuclear and New Energy Technology, Tsinghua University, Beijing 100084, PR China*
[b] *Department of Automotive Engineering and the State Key Laboratory of Automotive Safety and Energy, Tsinghua University, Beijing 100084, PR China*

Received 9 January 2006; received in revised form 28 February 2006; accepted 1 March 2006
Available online 17 April 2006

Abstract

Fuel cell modeling and simulation has aroused much attention recently because it can probe transport and reaction mechanism. In this paper, a computational fuel cell dynamics (CFCD) method was applied to simulate a proton exchange membrane fuel cell (PEMFC) stack for the first time. The air cooling mini fuel cell stack consisted of six cells, in which the active area was 8 cm^2 (2 cm × 4 cm). With reasonable simplification, the computational elements were effectively reduced and allowed a simulation which could be conducted on a personal computer without large-scale parallel computation. The results indicated that the temperature gradient inside the fuel cell stack was determined by the flow rate of the cooling air. If the air flow rate is too low, the stack could not be effectively cooled and the temperature will rise to a range that might cause unstable stack operation.

Keywords: Proton exchange membrane; Fuel cell; Stack; Modeling

1. Introduction

Proton exchange membrane fuel cells (PEMFCs) are promising power sources for stationary power stations, electric vehicles and portable devices [1]. Almost all key players in automobile manufacturing are now engaged in PEMFC vehicle development.

Since the pioneering work of Springer et al. [2] and Bernadi and Verbrugge [3], fuel cell modeling has attracted the research interest of many groups, because modeling could provide detailed transport and reaction information inside the fuel cells and guide the designs of fuel cell engineers. Costamagna and Srinivasan [4], Yao et al. [5], Wang [6], Bıyıkoğlu [7] and Faghri and Guo [8] have given good reviews on fuel cell modeling. Since Gurau et al. [9] introduced computational fluid dynamics (CFD) method into fuel cell modeling, CFD based fuel cell modeling has achieved great success and commercial CFD packages are available now. Wang [6] termed CFD coupled with fuel cell transport and reaction modeling as computational fuel cell dynamics (CFCD). To date, many papers on CFCD have been published for single cell modeling and simulation, some of which focused on the transport and reaction in a segment of the flow channel [10–12], and some others produced flow patterns [13,14]. There was no CFCD modeling or simulation work available in public documents for the fuel cell stack. One of the main difficulties in stack CFCD is the amount of computation needed. Including the flow channels in each cell plate of the stack, the computational gridpoints might be in the billions. In recent years, large-scale parallel computation has been successfully applied [15–18] in big area single fuel cell simulations. Wang and Wang [18] reported an ultra large-scale simulation with 23.5 million gridpoints, which was the largest scale computation reported. However, CFCD for fuel cell stack simulation is still difficult without simplification. In this paper, we present CFCD simulation results for a small PEMFC stack with reasonable simplification, which is the first report of a 3D CFD based fuel cell stack simulation.

2. Experimental

Fig. 1 shows a photograph of the experimental mini fuel cell stack with nine cells. E-Teck Pt/C catalyst (0.4 mg cm^{-2}), Toray carbon paper (190 μm thick) and homemade self-humidifying membrane (50 μm thick) were used to prepare the membrane electrolyte assemblies (MEAs). The active area was 8 cm^2 (2 cm × 4 cm). Graphite bipolar plates with straight air channels

* Corresponding author. Tel.: +86 10 62784827; fax: +86 10 62771150.
E-mail address: maozq@tsinghua.edu.cn (Z. Mao).

0378-7753/$ – see front matter © 2006 Elsevier B.V. All rights reserved.
doi:10.1016/j.jpowsour.2006.03.001

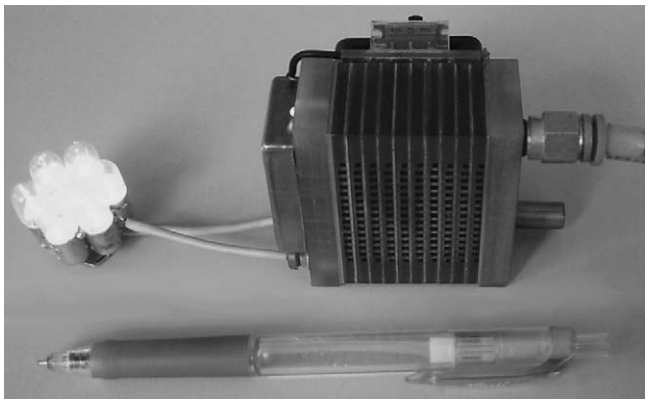

Fig. 1. Experimental mini fuel cell stack.

(width: 2 mm, depth: 2 mm) and a serpentine hydrogen channel (width: 2 mm, depth: 0.8 mm) were assembled in the stack. A micro-air fan was assembled in the stack to deliver air to the cells.

During the performance measurement, the stack was placed in a humidistat and an Arbin fuel cell test stand was used to collect performance data. The temperature and relative humidity of the air inside humidistat were adjusted to be 300 K and 80% relatively.

3. Model description

3.1. Model domain

The model domain is shown in Fig. 2. For the purpose of limiting the number of gridpoints to make the computation possible on a personal computer, six cells were simulated instead of nine cells as in the experimental stack. As shown in Fig. 2, the hydrogen and air manifolds were also included in the computation domain.

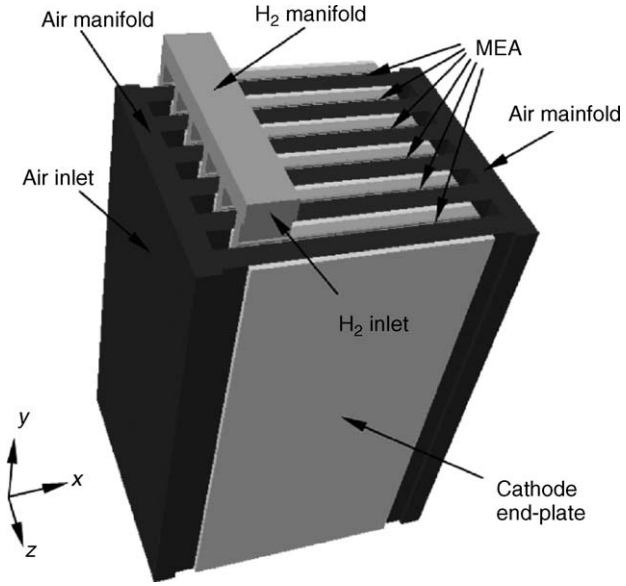

Fig. 2. Model domain of the fuel cell stack.

3.2. Model equations

Governing equations of the model employed in this work include conservation of mass, momentum, energy, species and current [19,20]:

Mass conservation equation:

$$\frac{\partial}{\partial t}(\varepsilon\rho) + \nabla\cdot(\varepsilon\rho U) = 0 \tag{1}$$

Momentum conservation equation:

$$\frac{\partial}{\partial t}(\varepsilon\rho U) + \nabla\cdot(\varepsilon\rho UU) = -\varepsilon\nabla p + \nabla\cdot(\varepsilon\tau) - \frac{\varepsilon^2\mu}{\kappa}U \tag{2}$$

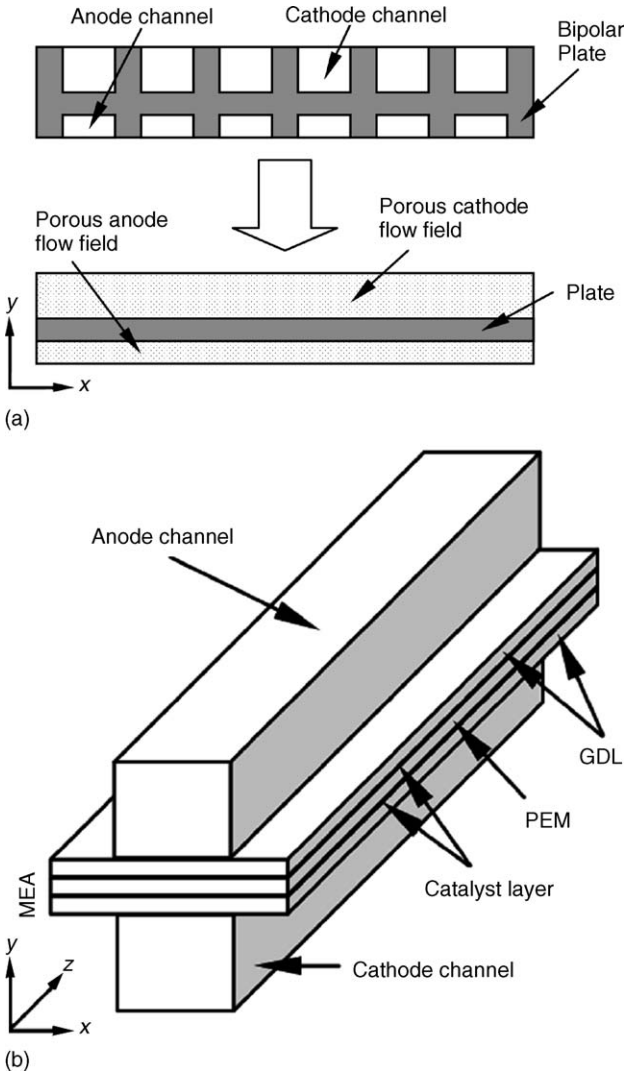

Fig. 3. (a and b) Simplification of the gas flow fields.

Energy conservation equation:

$$\frac{\partial}{\partial t}(\varepsilon\rho h) + \nabla\cdot(\varepsilon\rho U h) = \nabla\cdot q + \varepsilon\frac{\mathrm{d}p}{\mathrm{d}t} - j_{\mathrm{T}}\eta + \frac{i\times i}{\sigma} + \dot{S}_{\mathrm{h}} \tag{3}$$

Species conservation equation:

$$\frac{\partial}{\partial t}(\varepsilon\rho Y_i) + \nabla\cdot(\varepsilon\rho U Y_i) = \nabla\cdot J_i + \dot{\omega}_i \tag{4}$$

Current conservation:

$$\nabla\cdot(\sigma_{\mathrm{F}}\nabla\phi_{\mathrm{F}}) = -\nabla\cdot(\sigma_{\mathrm{S}}\nabla\phi_{\mathrm{S}}) = j_{\mathrm{T}} \tag{5}$$

And the Butler–Volmer equation for the electrochemical reaction:

$$j_{\mathrm{T}} = j_0\left[\exp\left(\frac{\alpha_{\mathrm{a}}F}{RT}\eta\right) - \exp\left(-\frac{\alpha_{\mathrm{c}}F}{RT}\eta\right)\right]\prod_{j=1}^{N}[\Lambda]^{\alpha_j} \tag{6}$$

More detail introduction of the model could be found in [20]. Liquid water is not taken into account and ideal gas law is applied.

3.3. Simplification and grids

For the purpose of reducing grids number, the flow fields were simplified to be porous media. As shown in Fig. 3, the bipolar plate with air and hydrogen flow fields was simplified to be two porous layers separated by a non-permeable plate. The porosity of the porous anode and cathode flow fields was set to be 0.67 because the flow channels took 2/3 of the total volume. Accordingly, the volume related parameters such as electric conductivity and thermal conductivity were set to be 1/3 of the graphite plate. Tortuosity of the cathode flow field was set to be 1.0 because the cathode flow channels were straight, and 1.5 was set for the anode. To simulate the pressure drop in the porous flow field, a section of fuel cell MEA with 10 cm straight channels (as shown in Fig. 3(b)) was modeled to collect the pressure drop data with different current density discharges. With the pressure drop data, Darcy's law was applied to calculate the permeability of the porous flow field:

$$\kappa = \frac{\mu L}{\Delta p}\cdot\frac{Q_{\mathrm{V}}}{S} \tag{7}$$

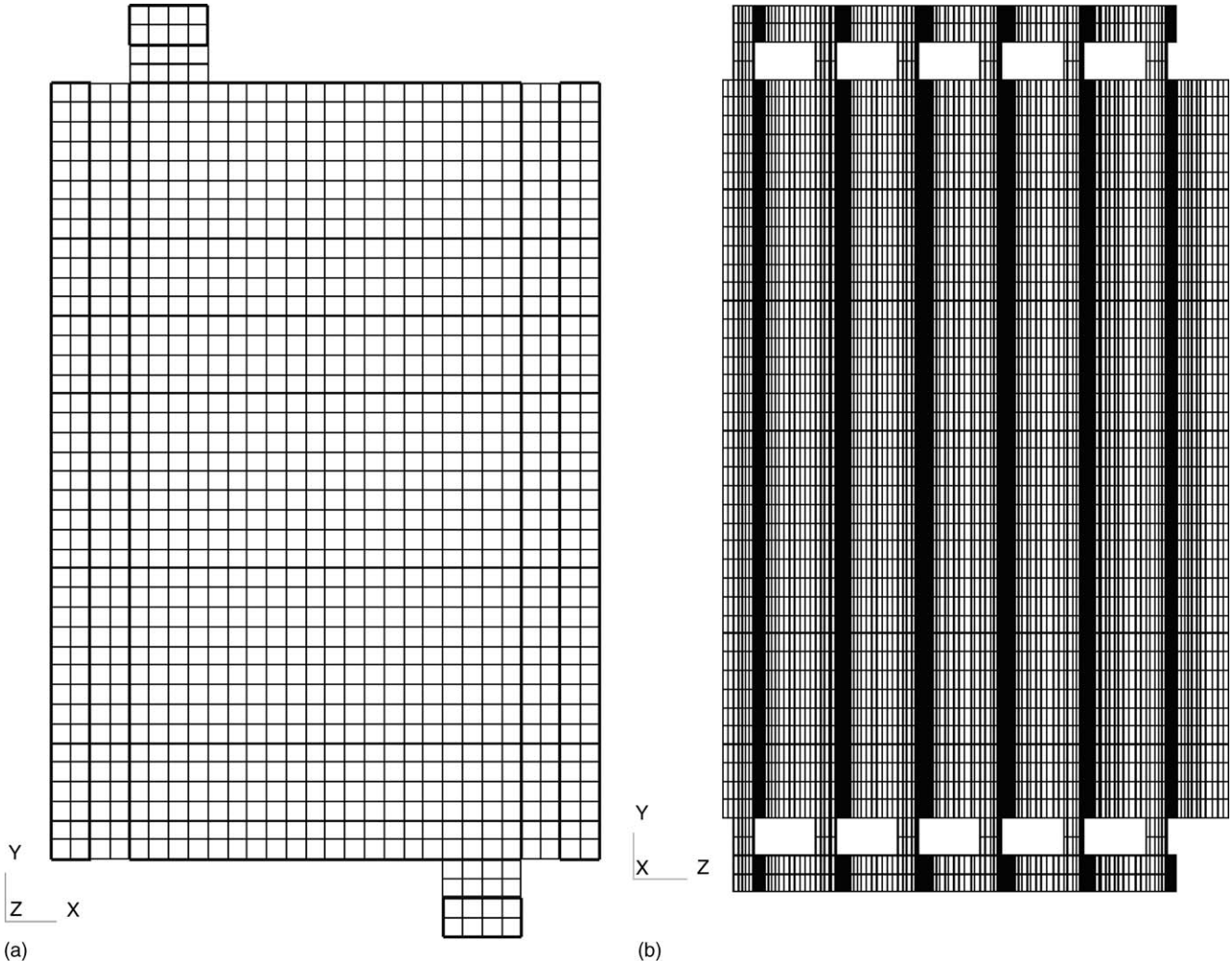

Fig. 4. Grids of the computational domain.

where κ is the permeability of the equivalent porous media (m^2); μ the viscosity of air (Pa s); L the channel length (m); Δp the pressure drop in the flow channel (Pa); Q_V the volume flux of air ($m^3\ s^{-1}$); and S is the section area of the flow channel (m^2). The calculated data did not vary quite much and an average value $2.4 \times 10^{-8}\ m^2$ was applied for the permeability of the anode and cathode porous flow fields.

The computation domain was discreted to generate structural grids with CFD-Micromesh®. The grids of the domain are shown in Fig. 4 in both *xy* and *yz* profiles. In *xy* profile, the plane was evenly discreted to cells with $1\ mm^2$ area. In *yz* profile, the grids were locally exponential distributed and there were 150 elements in *z* direction. With the flow channel been simplified to porous media, the grid number in *xy* profile could be reduced without taking the channel and rib width into account. The total grids were less than 200,000. Without the simplification, the grid number should be at least four times greater, which is beyond the computation capacity of a microcomputer.

3.4. Solution method

Parameters in the model are listed in Table 1. Anode inlet velocity is fixed to be $0.5\ m\ s^{-1}$, and the cathode inlet velocity varies with different operation conditions. Compared with the convective heat exchanging in the flow fields, heat dissipation by natural convection and radiation from the stack surface is relative small. Additionally, the end plate of the experimental stack is plastic and thermal conductivity is very small. So the surface walls of the computational domain were assumed to be adiabatic.

The problem was solved with CFD-ACE+ solver. A personal computer with Intel Pentium IV 2.4 GHz processor and 1.0 GB

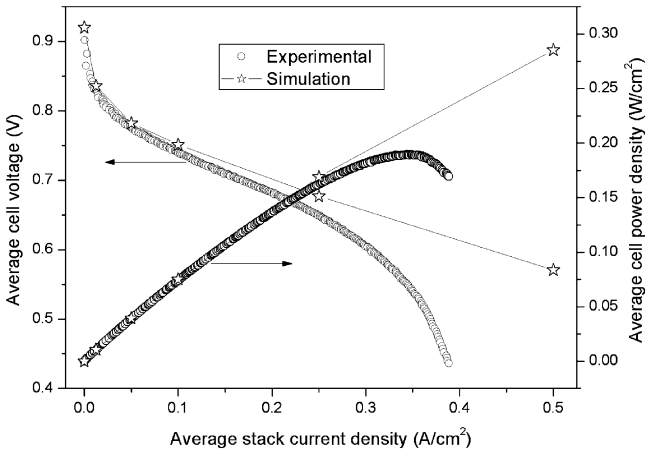

Fig. 5. *I–V* and *I–P* curves of the stack.

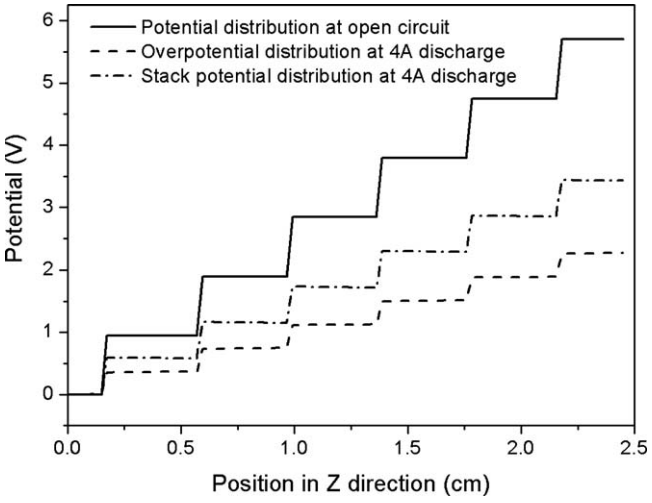

Fig. 6. Potential distribution across the fuel cell stack at 4 A discharge.

Table 1
Parameters in the model

Parameters	Value	Parameters	Value
Thickness		Thermal conductivity	
Cathode flow field	2 mm	Plate	$129\ W\ (m\ K)^{-1}$
Anode flow field	0.5 mm	Flow field	$43\ W\ (m\ K)^{-1}$
Plate	0.5 mm	GDL and CL	$21\ W\ (m\ K)^{-1}$
Gas diffusion layer (GDL)	200 μm	PEM	$0.67\ W\ (m\ K)^{-1}$
Catalyst layer (CL)	25 μm	Electric conductivity	
Proton conducting membrane (PEM)	50 μm	Plate	$3000\ S\ m^{-1}$
Porosity		Flow field	$1000\ S\ m^{-1}$
Flow field	0.67	GDL and CL	$1250\ S\ m^{-1}$
GDL	0.6	PEM	$1.8 \times 10^{-20}\ S\ m^{-1}$
CL	0.5	Ionic conductivity	
PEM	0.28	CL	$4.2\ S\ m^{-1}$
Tortuosity		PEM	Eq. from [2]
GDL and CL	1.5	Exchange current density	
PEM	10	H_2 oxidation	$1.0 \times 10^{9}\ A\ m^{-3}$
Cathode flow field	1.0	O_2 reduction	$2.0 \times 10^{5}\ A\ m^{-3}$
Anode flow field	1.5	Operation condition	
Permeability		H_2/air temperature	300 K
Flow field	$2.4 \times 10^{-8}\ m^2$	H_2/air relative humidity	80%
GDL and CL	$1.76 \times 10^{-11}\ m^2$	Outlet H_2/air pressure	0.1 MPa
PEM	$1.8 \times 10^{-18}\ m^2$		

RAM was adopted for the computation. The calculation converged after around 2500 iterations and took around 30 h for each case.

4. Results and discussions

Fig. 5 compares the averaged cell *I–V* and *I–P* curves of the stack from simulation and experiments. In many models, the thermodynamic potential was applied to calculate the open circuit voltage (OCV) of the fuel cell [21,22]; some authors used empirical equations to calculate this parameter [23]. OCV calculated from these methods is higher than 1.1 V for normal fuel cell operation conditions. However, normally cell OCV is not higher than 1.0 V in experiments. In this model, 0.92 V average cell OCV from experiments is used. In Fig. 5, it can be seen that the simulation curves are in good accordance with the experimental curves when the current density is relatively low. In the high current density region, the experimental *I–V* curve deviates greatly from linear relation, while the simulation curve shows good linear behavior. The performance curves show a great difference in the high current density region. One of the reasons for this difference is that current density beneath the ribs

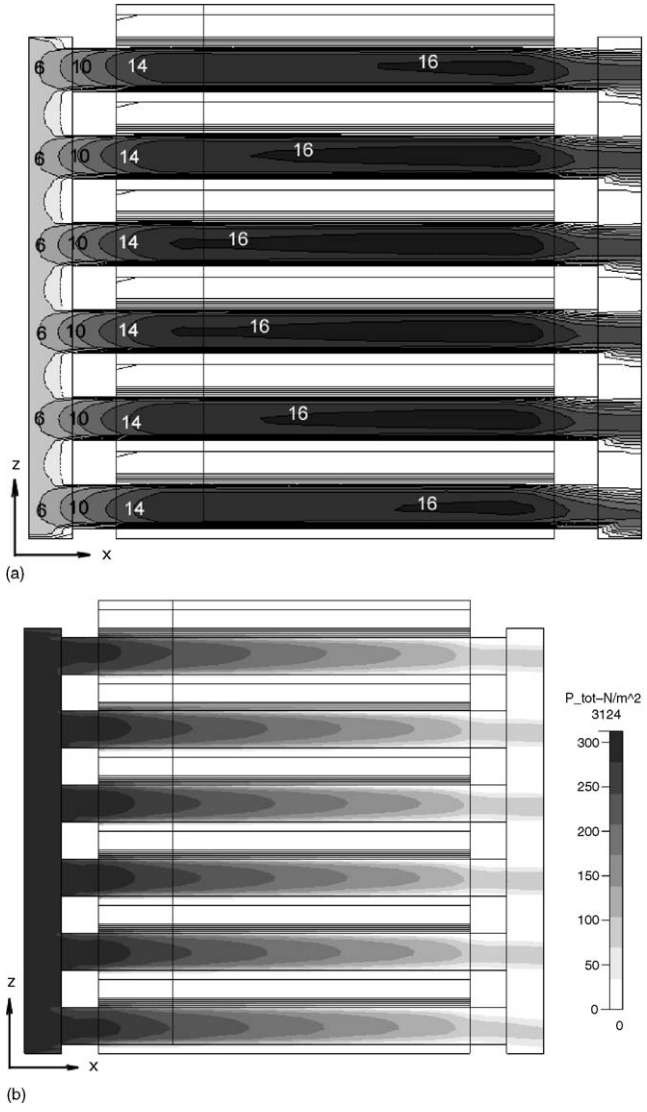

Fig. 7. Velocity and pressure distribution in the stack at 4 A discharge. (a) Air velocity (m s^{-1}) and (b) total pressure (Pa).

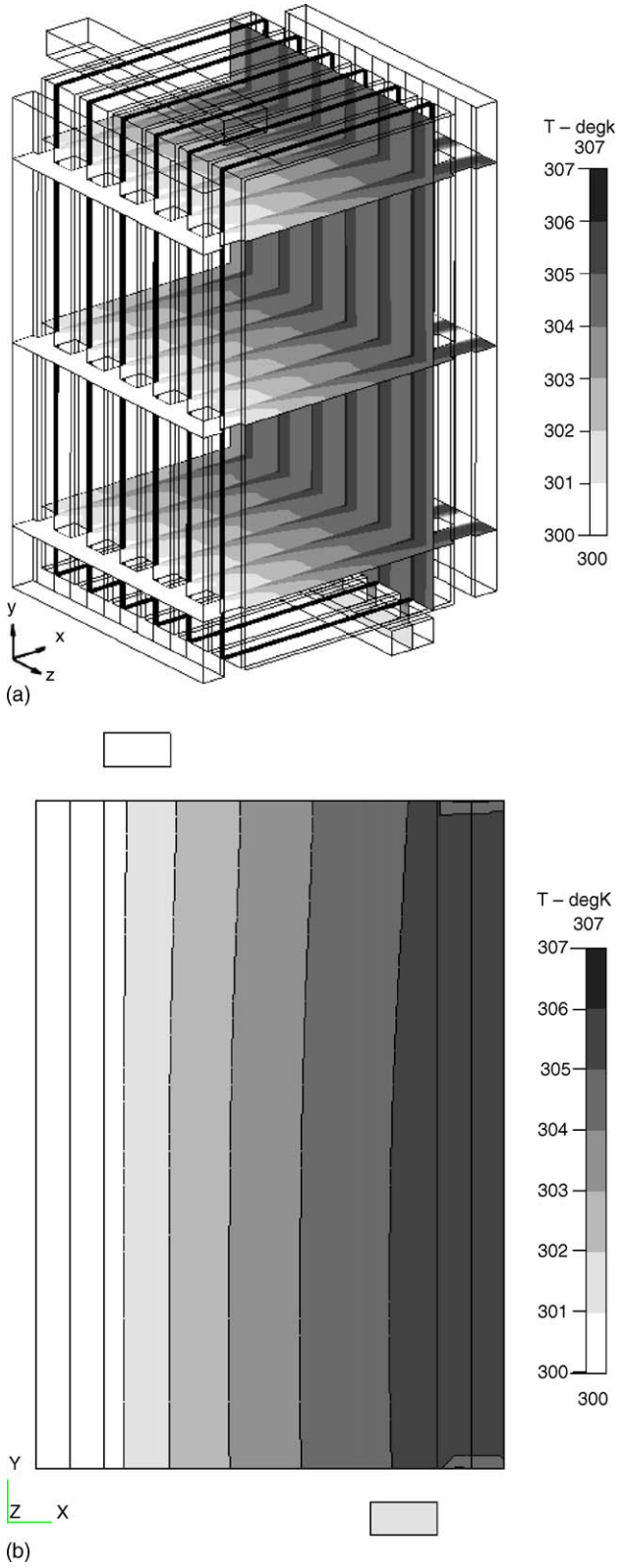

Fig. 8. Temperature distribution of the fuel cell stack in *xz* and *yx* section planes (a) and in *xy* section plane (b) with 5 m s^{-1} air inlet velocity and 4 A discharge.

is much lower than that beneath the channel when the fuel cell operates in the low voltage region [22]. But in the simulation, because the flow field is simplified to be a porous media, the influence of the rib is neglected. Another reason might be liquid water flooding, especially for the GDL beneath the bipolar plate ribs.

The potential distribution inside the stack at 4 A discharge is shown in Fig. 6. The distribution information is given along

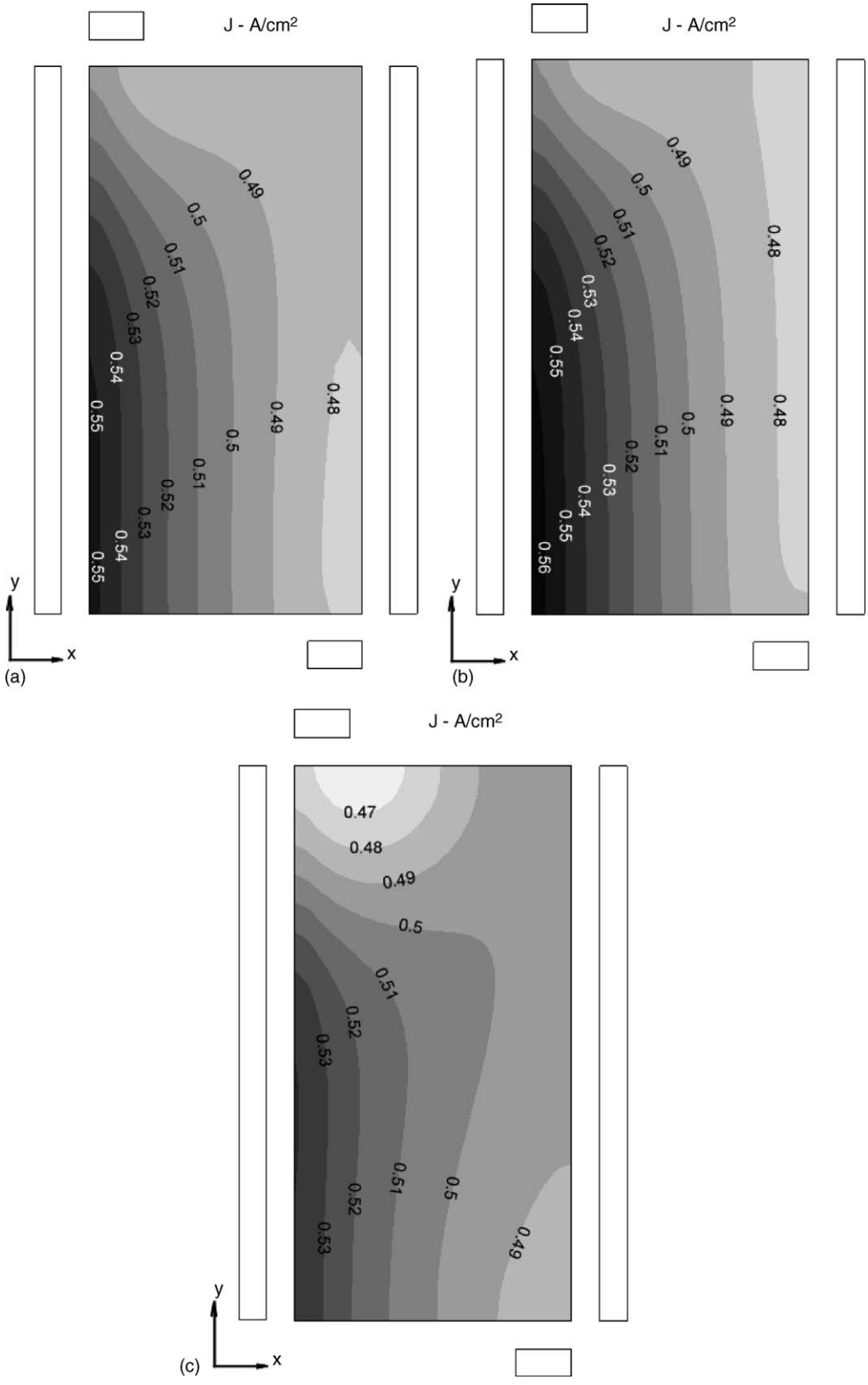

Fig. 9. Current density (A cm^{-2}) in the membrane: (a) cell 1; (b) cell 3; (c) cell 6.

the intersection line of *xz* and *yz* section planes across the central point of the computational domain. Potential of the anode side end plate is set to zero and as a reference potential, then the potential and overpotential are given according to the reference potential. The positions where the potentials jump-up correspond to the positions of MEAs in the stack. Activation overpotential in the catalyst layers (especially in cathode catalyst layers) and ionic impedance in PEM are the main causes of overpotential across the stack. The ohmic overpotential in the GDLs and bipolar plates is much smaller than the former two.

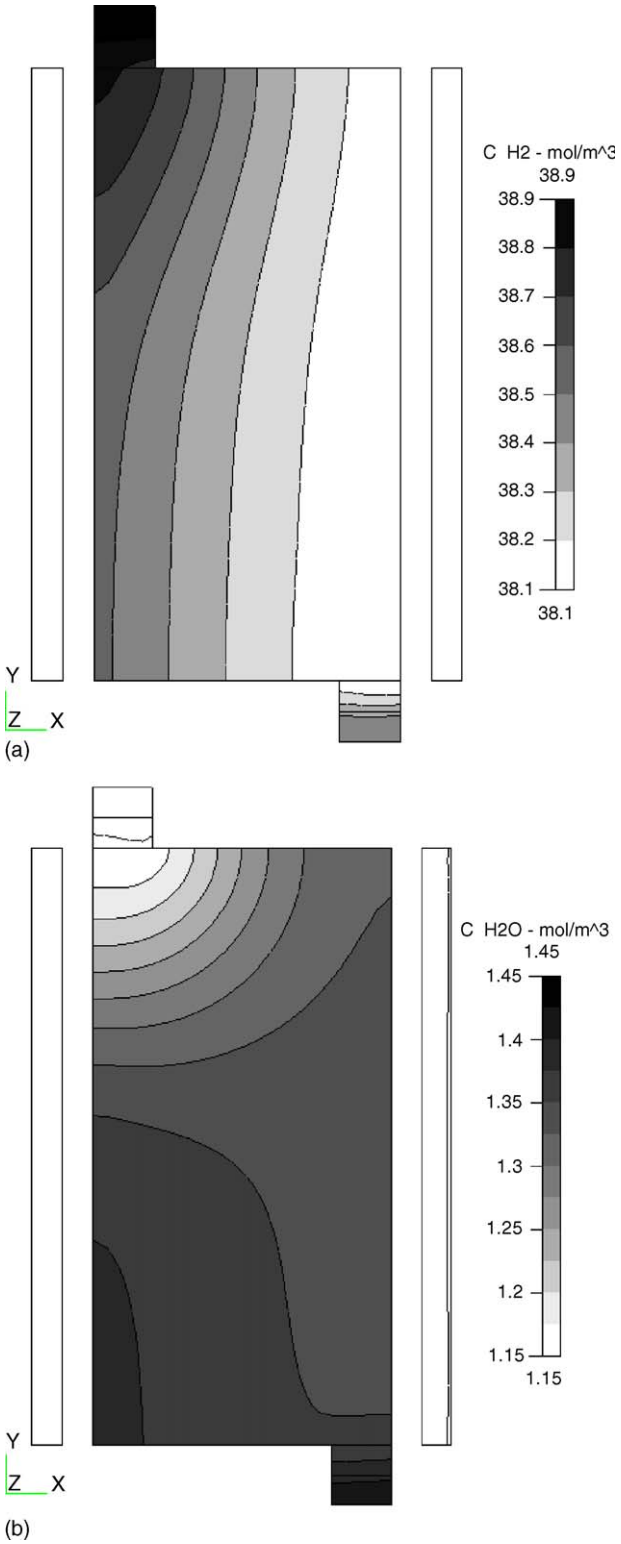

Fig. 10. Hydrogen (a) and water (b) molar concentrations in anode flow field of cell 3.

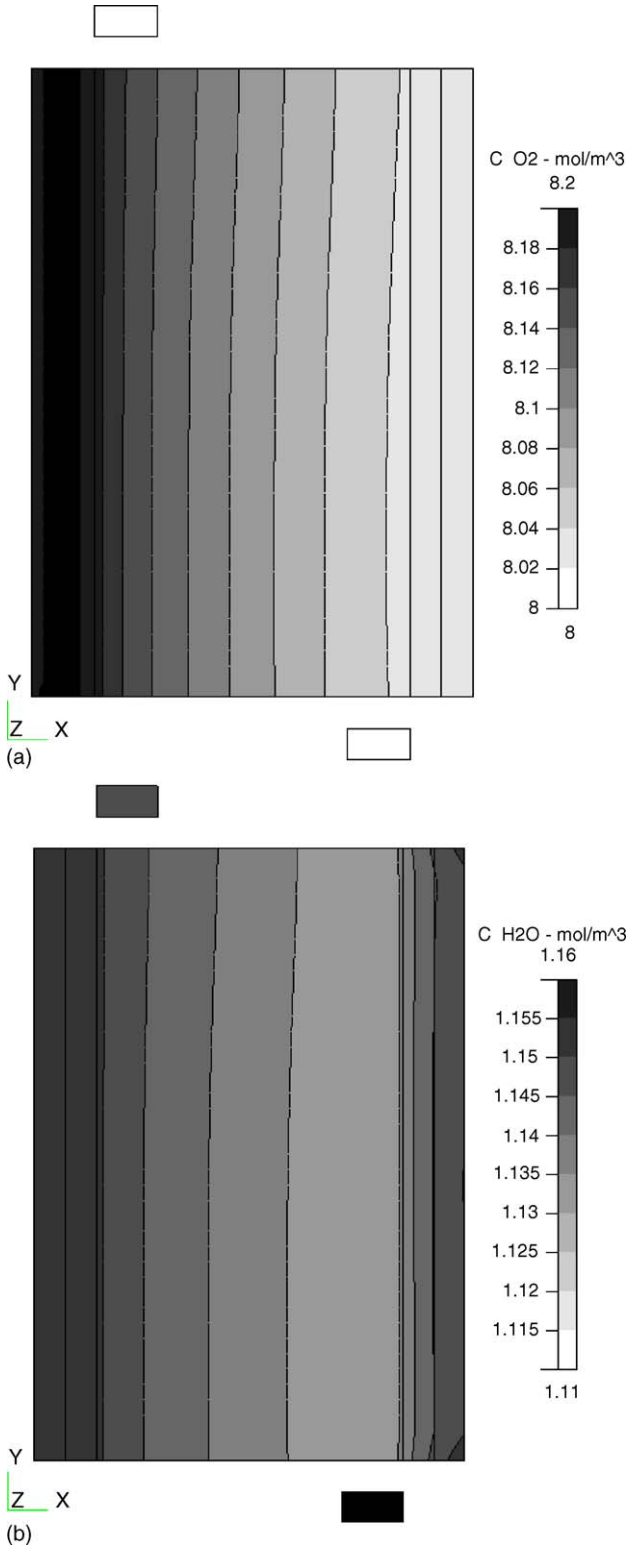

Fig. 11. Oxygen (a) and water (b) molar concentrations in cathode flow field of cell 3.

With the solid phase conductivity data listed in Table 1, it is estimated that the electric resistance of the stack is about 30 mΩ and ohmic overpotential is 120 mV at 4 A discharge. From the simulated polarization curve shown in Fig. 5, the stack resistance could be calculated with a nonlinear fit of the Tafel equation shown below:

$$E = E_0 + B\log i - R \cdot i \tag{8}$$

The overall stack resistance is fitted to be 256 mΩ, which reveals that the membrane ionic resistance is about seven times greater than the electric resistance. The electric overpotential, ionic overpotential and activation overpotential are calculated to be 0.12 V, 1.023 V and 2.285 V, respectively. Activation takes most part of the stack overpotential.

Fig. 7(a and b) shows the air velocity and total pressure distribution in the stack, respectively. The air inlet velocity is 5 m s^{-1} and the stack current is 4 A. It could be seen that the air flow rate increases along the ducts, which is because the water production and temperature increase along the flow direction. The highest speed could be 16.87 m s^{-1}. The total pressure distribution is shown in plot (b). It shows that the total pressure loss is 312.4 Pa, which includes 294.6 Pa static pressure loss and 17.8 Pa dynamic pressure loss ($\rho u^2/2$). The dynamic pressure loss is much smaller than the static pressure loss because of the low density of air.

The main issue for an air cooling stack is not the pressure loss but the effectiveness of stack cooling. With higher stack temperature, water is easier to evaporate because the saturation vapor pressure of water is higher. The membrane will be inclined to dehydrate and lose ionic conductivity, which will make the fuel cell performance deteriorate. In fact, air cooling stacks without external humidification could not be steadily operated when stack temperature is above 323 K [24]. Fig. 8 shows temperature distribution in the fuel cell stack with 5 m s^{-1} air inlet velocity and 4 A discharge. Plot (a) shows temperature in *yz* and *xz* section planes and (b) in *xy* section plane across the air flow field of cell 3 (numbered from the anode side). The plots show small temperature gradient in *y* direction, but great gradient in *x* and *z* directions. Temperature in MEAs is higher than that in the flow field, which could be seen clearer in Fig. 13. For 4 A discharge and 5 m s^{-1} air inlet velocity, air temperature increases about 5 K from the air inlet to the air outlet.

Current density distributions in the membrane of cells 1, 3 and 6 are shown in Fig. 9. Although current density distributions show some small difference in different cells, the distribution trend is similar in every cell: current density decreases from the air inlet to the outlet, and increases to some extent from hydrogen inlet to outlet. The highest current density regions appear on the air inlet side and away from the hydrogen inlet side. One may doubt the distribution trend with some reasons: firstly, oxygen reduction reaction (ORR) kinetics will increase along the air flow direction because cell temperature increases from air inlet to outlet as shown in Fig. 8(b); secondly, water concentration seems to be higher on the air outlet side because of water production. As a result, it seems that current density should be higher on the air outlet side rather than the inlet side. Thirdly, membrane conductivity seems to increase along *x* direction because membrane conductivity is higher under higher temperature according to Eq. (9) [2], where σ is membrane conductivity and λ is membrane water content:

$$\sigma = (0.005139\lambda - 0.00326)\exp\left[1268\left(\frac{1}{303} - \frac{1}{T}\right)\right] \tag{9}$$

This argument sounds like reasonable, but there are some more important reasons. For the first point, it should be noted that the influence of temperature to ORR kinetics is not considered in the present model. With Eq. (10) as given in [22], ORR exchange current density increases 20% when temperature increases from 300 K to 305 K.

$$i_{0,2} = i_{0,1}\exp\left[-\frac{\Delta E}{R}\left(\frac{1}{T_2} - \frac{1}{T_1}\right)\right] \tag{10}$$

Although this omission will cause some influence, it is not the main reason for the current distribution. Otherwise, there would not be a great current density gradient shown in the *y* direction (Fig. 9), because almost no temperature gradient is shown in this direction (Fig. 8(b)). The current density gradient in the *y* direction indicates that the fuel cell reaction is more sensitive to humidity than ORR kinetics. In Fig. 10, molar concentrations of hydrogen and water in hydrogen flow field of cell 3 are shown. It should be noted that water concentration is highest in the left-bottom corner, where the highest current density is shown.

Secondly, because the air stoichiometry is quite large, very small oxygen and water concentration gradients are shown. In

Fig. 12. Membrane water content of cell 3 at 4 A discharge.

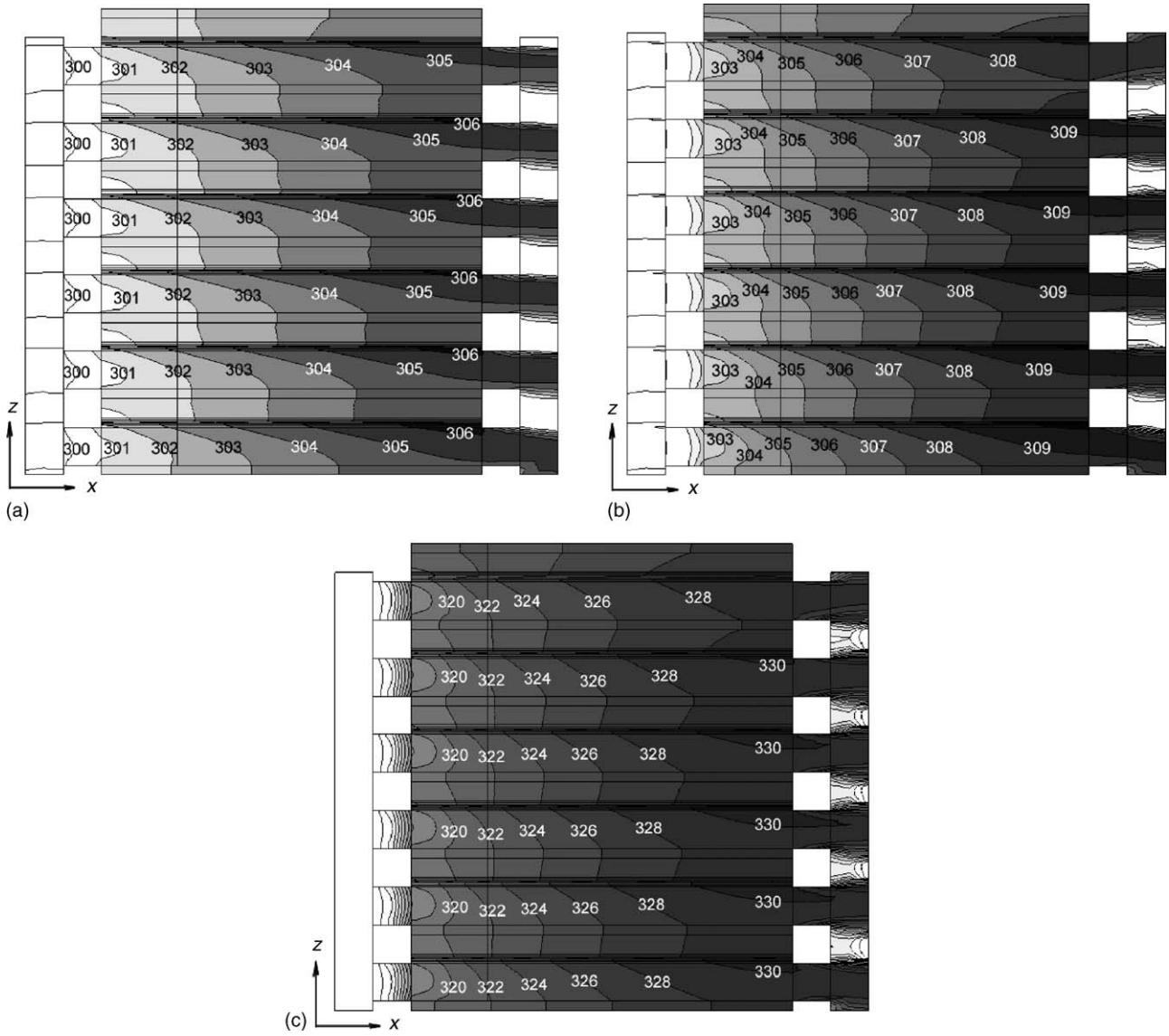

Fig. 13. Temperature distribution of the stack with different air inlet velocities in *xz* section plane: (a) 5 m s^{-1}; (b) 3 m s^{-1}; (c) 1 m s^{-1}.

Fig. 11, oxygen and water concentrations in air flow field of cell 3 are shown. With 5 m s^{-1} air inlet velocity, air flux is calculated to be 274 L min^{-1}, while the stoichiometric air flux for 4 A operation is 434 mL min^{-1}, which indicates that the air is 630 times in excess. Although with water production from the electrochemical reaction, the water concentration is actually shown to decrease in the *x* direction because of the gas density decrease with the increase of temperature.

Thirdly, it is true that temperature will influence the membrane conductivity, but it will influence the membrane water content λ greater. Although water concentration gradients are not great in Figs. 10(b) and 11(b), water humidity will decrease in *x* direction with the increase of temperature. When temperature increases from 300 K to 305 K, air relative humidity will decrease from 80% to 60.2% because of the 32.7% increase of saturated vapor pressure. So water activity on both anode and cathode sides will vary quite much in *x* direction according to local temperatures, which will in turn impact the mem-

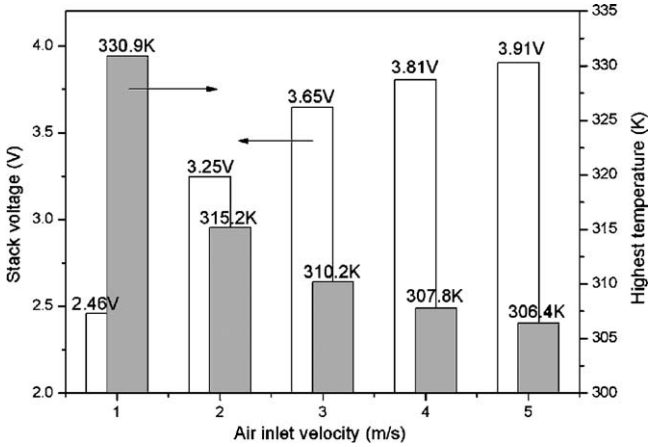

Fig. 14. Voltage and highest temperature in stack at different air inlet velocities at 4 A discharge.

brane water content. Fig. 12 shows the membrane water content for 5 m s^{-1} air inlet velocity and 4 A discharge. A large gradient of membrane water content is shown in this plot. It could also be seen that the water content distribution is very similar to that of the current density distribution shown in Fig. 9(b).

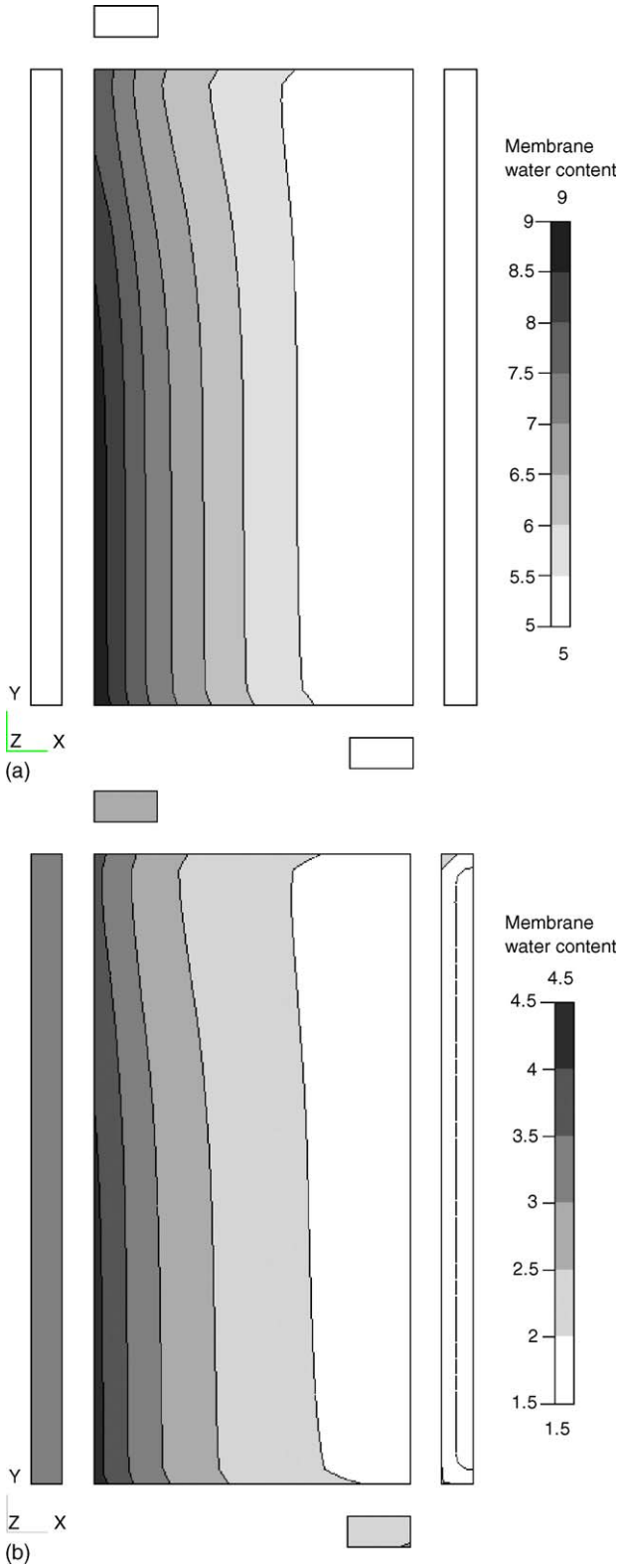

Fig. 15. Membrane water content of cell 3 at 4 A discharge. Air inlet velocity: (a) 2 m s^{-1} and (b) 1 m s^{-1}.

With the premise of effective stack cooling, a lower air flow rate will reduce the power consumption of the blower and increase the system efficiency. Different air flow rate cases were studied to determine the effectiveness of cooling. The air inlet velocity is specified to be 5–1 m s^{-1} and results are shown in Figs. 13 and 14. In Fig. 13, temperature distributions in *xz* profile through the central point are shown in contour plots with air inlet velocity 5 m s^{-1}, 3 m s^{-1} and 1 m s^{-1}, respectively. From these plots it could be seen that the isothermal curves form peaks at the positions of MEAs and large temperature gradients are shown in the membranes. In the cathode catalyst layers, water is produced and releases heat, so the temperatures in the cathode catalyst layers are the highest at the same position along the flow direction. The membranes have the lowest thermal conductivity and large temperature differences are shown on double sides of the membranes. The air inlet velocity decreases from 5 m s^{-1} to 3 m s^{-1}, the highest stack temperature increases from 306 K to 310 K. While the inlet velocity decreases to 1 m s^{-1}, the highest temperature increases to about 330 K. In Fig. 14, the highest stack temperatures and stack voltages are shown according to different air inlet velocities. For the case of 1 m s^{-1}, the air flux is too small for the stack cooling and the stack temperature is higher than 323 K. For the case of 2 m s^{-1}, the air is about 250 times in excess and the stack temperature is less than 323 K. Fig. 15 shows membrane water content of cell 3 with 2 m s^{-1} and 1 m s^{-1} air inlet velocity at 4 A discharge. It could be seen that the water content is in a range 5–9; but when inlet velocity decreases to be 1 m s^{-1}, membrane water content decreases to very low, less than 4.5. At this time, the fuel cell membrane will dry out and could not operate steadily. In experiments the fuel cell stack performance will decrease sharply when the air flow rate is not enough. For 2 m s^{-1} air inlet velocity, although the stack power is relative low, 11–13.7 W at 5 m s^{-1} inlet velocity is the choice for stack operation. It needs to be pointed out that, because the cell temperature varies with stack current, for a better stack temperature management, it is better to adjust the air flow rate according to the load.

5. Conclusion

A mini PEMFC stack was simulated three dimensionally with a reaction and transport coupled CFCD model. With reasonable simplification, gridpoints of the computational domain could be effectively reduced and allow a full 3D fuel cell stack computation to be conducted in personal computers. The simulation results were compared with experimental results and reasonable agreement was found. Temperature distributions in the stack with different air flow rates were given and the results show that, for 4 A operation, the air inlet velocity could be as low as 2 m s^{-1} (250 times excess) and allow the stack to be effectively cooled, while for 1 m s^{-1}, the membrane water content was too low to keep the stack in steady operation. The simulation results illustrate a method for large-scale fuel cell stack simulation.

Acknowledgements

Financial supports by "National 973 Project on Hydrogen Energy (TG2000026410)" and "Open Fund of State Key Laboratory of Automotive Safety and Energy (KF2005-012)" are gratefully acknowledged.

References

[1] Z.Q. Mao, Fuel Cells, Chemical Industry Press, Beijing, 2005.
[2] T.E. Springer, T.A. Zawodzinski, S. Gottesfeld, Polymer electrolyte fuel cell model, J. Electrochem. Soc. 138 (1991) 2334–2342.
[3] D.M. Bernardi, M.W. Verbrugge, Mathematical model of the solid-polymer-electrolyte fuel cell, J. Electrochem. Soc. 139 (1992) 2477–2491.
[4] P. Costamagna, S. Srinivasan, Quantum jumps in the PEMFC science and technology from the 1960 to the year 2000. Part II. Engineering, technology development and application aspects, J. Power Sources 102 (2001) 253–269.
[5] K.Z. Yao, K. Karan, K.B. McAuley, et al., A review of mathematical models for hydrogen and direct methanol polymer electrolyte membrane fuel cells, Fuel Cells 4 (2004) 3–29.
[6] C.Y. Wang, Fundamental models for fuel cell engineering, Chem. Rev. 104 (2004) 4727–4766.
[7] A. Bıyıkoğlu, Review of proton exchange membrane fuel cell models, Int. J. Hydrogen Energy 30 (2005) 1181–1212.
[8] A. Faghri, Z. Guo, Challenges and opportunities of thermal management issues related to fuel cell technology and modeling, Int. J. Heat Mass Transfer 48 (2005) 3891–3920.
[9] V. Gurau, H.T. Liu, S. Kakac, Two-dimensional model for proton exchange membrane fuel cells, AIChE J. 44 (1998) 2410–2422.
[10] K.W. Lum, J.J. McGuirk, Three-dimensional model of a complete polymer electrolyte membrane fuel cell—model formulation, validation and parametric studies, J. Power Sources 143 (2005) 103–124.
[11] T. Berning, N. Djilali, A 3D, multiphase, multicomponent model of the cathode and anode of a PEM fuel cell, J. Electrochem. Soc. 150 (2003) A1589–A1598.
[12] Y. Wang, C.Y. Wang, Transient analysis of polymer electrolyte fuel cells, Electrochim. Acta 50 (2005) 1307–1315.
[13] S.W. Cha, R. O'Hayre, Y. Saito, et al., The sacling behavior of flow patterns: a model investigation, J. Power Sources 134 (2004) 57–71.
[14] S. Dutta, S. Shimpalee, J.W. Van Zee, Numerical prediction of mass-exchange between cathode and anode channels in a PEM fuel cell, Int. J. Heat Mass Transfer 44 (2001) 2029–2042.
[15] S. Shimpalee, S. Greenway, D. Spuckler, et al., Predicting water and current distributions in a commercial-size PEMFC, J. Power Sources 135 (2004) 79–87.
[16] H. Meng, C.Y. Wang, Large-scale simulation of polymer electrolyte fuel cells by parallel computing, Chem. Eng. Sci. 59 (2004) 3331–3343.
[17] Y. Wang, C.Y. Wang, Simulation of flow and transport phenomena in a polymer electrolyte fuel cell under low-humidity operation, J. Power Sources 147 (2005) 148–161.
[18] Y. Wang, C.Y. Wang, Ultra large-scale simulation of polymer electrolyte fuel cells, J. Power Sources 153 (2006) 130–135.
[19] Y. Wang, C.Y. Wang, Modeling polymer electrolyte fuel cells with large density and velocity changes, J. Electrochem. Soc. 152 (2005) A445–A453.
[20] S. Mazumder, J.V. Cole, Rigorous 3-D mathematical modeling of PEM fuel cells I. Model predictions without liquid water transport, J. Electrochem. Soc. 150 (2003) A1503–A1509.
[21] J.C. Amphlett, R.M. Baumert, R.F. Mann, et al., Performance modeling of the Ballard Mark IV solid polymer electrolyte fuel cell I. Mechanistic model development, J. Electrochem. Soc. 142 (1995) 1–8.
[22] W. Sun, B.A. Peppley, K. Karan, An improved two-dimensional agglomerate cathode model to study the influence of catalyst layer structural parameters, Electrochim. Acta 50 (2005) 3359–3374.
[23] S. Um, C.Y. Wang, K.S. Chen, Computational fluid dynamics modeling of proton exchange membrane fuel cells, J. Electrochem. Soc. 147 (2000) 4485–4493.
[24] C. Wang, Studies on the self-humidifying proton exchange membrane fuel cell, Ph.D. Dissertation, Tsinghua University, Beijing, 2003.